Materials Advances

ROYAL SOCIETY OF CHEMISTRY

PAPER

View Article Online
View Journal | View Issue

Cite this: *Mater. Adv.*, 2026, 7, 1203

Ni–Cu–Mn based hybrid supercapacitor with high flexibility and strength for wearable electronics

Arunesh Kumar,[a] Arpit Thomas,[b] Michael Lastovich,[c] Bharat Gwalani[c] and Harpreet Singh Arora *[a]

Flexible supercapacitors are gaining huge attention as energy storage devices for wearable and portable electronics, owing to their lightweight nature, mechanical flexibility, high power output, and long operational lifespan. Their ability to maintain performance under bending and deformation makes them highly suitable for integration into next-generation flexible systems. However, flexible supercapacitor devices based on conventional polymers often struggle to maintain a balanced performance between flexibility and energy storage capability. Herein, we report the excellent performance of a NiCuMn oxide (NCM/O) based highly flexible hybrid supercapacitor (FHS). NCM/O powders were produced using a facile dealloying approach, resulting in a flaky nanoporous structure. The FHS showed a high areal capacitance of 414.6 mF cm^{-2} at 1 mA cm^{-2} and retained more than 75% of its capacitance even at a high current density of 6 mA cm^{-2}. The fabricated symmetric FHS demonstrated a notable energy density of 129.58 μWh cm^{-2} at a power density of 750 μW cm^{-2}. It also exhibited outstanding long-term stability, retaining 94.7% of its initial capacitance after 10 000 charge–discharge cycles. Additionally, the device maintained stable electrochemical performance under various bending conditions, confirming its mechanical flexibility. Owing to these promising results, the in-house developed large flexible supercapacitor was used as a wristwatch strap, where it functioned reliably for several consecutive days.

Received 14th October 2025,
Accepted 7th December 2025

DOI: 10.1039/d5ma01187f

rsc.li/materials-advances

1. Introduction

The rapid advancement and widespread adoption of flexible and wearable electronics in modern society have spurred an urgent demand for efficient, lightweight, and flexible energy storage systems. Among the various available technologies, flexible supercapacitors have emerged as a highly promising class of energy storage devices, primarily due to their unique advantages including high power density, rapid charge–discharge capability, long cycle life, and robust mechanical flexibility.[1–4] These characteristics make them ideal candidates for integration into next-generation portable and wearable systems. Nevertheless, achieving flexible supercapacitors with both high energy and power densities remains a significant technical hurdle. Overcoming this challenge is largely governed by the design and development of suitable electrode materials, which are fundamental to the overall electrochemical performance of supercapacitors.[5–7]

The selection of a suitable electrode material is critical, as it directly influences the capacitance, rate performance, and long-term stability of the device. Carbon-based materials such as graphene, carbon nanotubes, and activated carbon have been widely employed due to their high electrical conductivity and large specific surface area.[8,9] However, these materials primarily store charge through the electric double-layer capacitance (EDLC) mechanism, which restricts their energy density. Conducting polymers, including polyaniline and polypyrrole, can generally contribute to pseudo-capacitance *via* faradaic redox reactions, thereby offering higher capacitance values.[10,11] Yet, these materials often exhibit poor electrical conductivity and suffer from significant volume changes during cycling, leading to mechanical degradation and limited lifespan.

Transition metal oxides (TMOs) have gained considerable attention as alternative electrode materials for supercapacitors. Their high theoretical capacitance, owing to reversible faradaic redox reactions and multiple oxidation states, along with good chemical stability, makes them promising candidates. TMOs such as RuO_2, MnO_2, NiO, and Co_3O_4 have shown encouraging electrochemical performance.[12–15] However, their practical implementation, especially in flexible devices, is hampered by inherent limitations such as low intrinsic electrical conductivity and mechanical brittleness, which impair their rate capability and flexibility under mechanical stress. To overcome these

[a] *Department of Mechanical Engineering, Shiv Nadar Institution of Eminence, Deemed to be University, UP, 201310, India. E-mail: harpreet.arora@snu.edu.in*
[b] *Centre for Inter-Disciplinary Research and Innovation, University of Petroleum and Energy Studies, Bidholi Via-Prem Nagar, Dehradun, 248007, India*
[c] *Department of Materials Science and Engineering, North Carolina State University, Raleigh, North Carolina, 27695, USA*

shortcomings, recent research has focused on multielement transition metal oxides (MTMOs). By integrating different metal cations into a single oxide matrix, MTMOs can leverage synergistic interactions between the constituent metals. This multicomponent strategy can enhance electronic conductivity, increase electrochemical activity, and improve structural robustness during charge–discharge cycling. Consequently, MTMOs hold great potential for fabricating high-performance, flexible supercapacitor electrodes.[16–18]

Among various synthesis techniques for producing such materials—such as sol–gel processing, hydrothermal methods, and electrodeposition—dealloying stands out as a particularly effective approach.[19,20] Unlike traditional methods that often require complex procedures, prolonged reaction times, and multistep treatments, dealloying offers a relatively simple, one-step route to create nanostructured, porous oxide architectures.[21] This method involves the selective removal of less noble elements from an alloy, resulting in highly porous frameworks with large surface areas and interconnected ion/electron pathways. These structural features not only promote rapid charge transport and ion diffusion but also enhance the overall electrochemical efficiency of the resulting electrodes.

In this study, we successfully fabricated a flexible hybrid supercapacitor (FHS) using a straightforward dealloying approach. A bulk NiCuMn alloy was selectively dealloyed to remove Mn, resulting in a nanostructured, flaky oxide powder composed of Ni, Cu and Mn oxides. This powder was drop-cast onto a 20 μm thin stainless-steel mesh (SM) to form a flexible electrode. The electrode exhibited outstanding energy storage performance, attributed to the synergistic contribution of the TMOs. A symmetric FHS device was assembled, demonstrating remarkable energy and power densities along with excellent cycling stability. To evaluate practical applicability, two FHS units were connected in both series and parallel configurations. Furthermore, the device was electrochemically tested under various bending conditions, showing minimal deviation in cyclic voltammetry behavior, highlighting its potential for wearable electronics. Finally, large-area electrodes were fabricated and used as a wristwatch strap, underscoring the real-world applicability of the developed flexible supercapacitor.

2. Experimental section

2.1 Materials

$Ni_{15}Cu_{15}Mn_{70}$ alloy casting (NCMAC), stainless steel mesh (SM), potassium hydroxide (KOH), pellets (purity 99.98%, Thermo Fisher Scientific), ammonium sulphate ($(NH_4)_2SO_4$) (purity 99.99%, Sigma-Aldrich), polyvinylidene fluoride (PVDF, Sigma-Aldrich), super P carbon (purity 99+%, Thermo Fisher scientific), *N*-methyl-2-pyrrolidone (NMP, Matlabs technologies), and hydrogen fluoride (HF, 40%, Fisher Scientific) were used.

2.2 Synthesis of NiCuMn–oxide (NCM/O) powder

The synthesis of NCM/O powder involves a single-step electrochemical dealloying process. The NCMAC alloy was sectioned into 100 μm thick sheets using wire electrical discharge machining (WEDM) and subsequently dealloyed in 2 M $(NH_4)_2SO_4$ solution at 90 °C for 2 h. Dealloying is an electrochemical process in which the less noble element is selectively leached out from the alloy matrix. In this process, Mn, being less noble, is preferentially leached out during dealloying in $(NH_4)_2SO_4$ solution, resulting in the formation of NCM/O powder. The recovered powder was then thoroughly cleaned with ethanol and deionized water, followed by drying in a vacuum oven at 70 °C for 24 hours.

2.3 Synthesis of the SM//NCM/O electrode

SM was ultrasonically cleaned in both HF and DI water for 15 minutes each at 40 °C and then dried in a vacuum oven. The as-prepared NCM/O powder was thoroughly mixed with Super P carbon and PVDF in an 8 : 1 : 1 ratio. Subsequently, the mixture was dispersed in NMP solution to form a uniform slurry, which was then drop-cast onto a cleaned 20 μm thin SM substrate (shown in Fig. S1) followed by drying in a vacuum oven.

2.4 Material characterization

The NCM/O powder sample was analysed using a field emission scanning electron microscope (FESEM) (JEOL JSM-7610F Plus) and transmission electron microscope (TEM) (FEI Titan 80-300) operated at 200 kV. An X-ray diffractometer (XRD) (Bruker D8 Discover) fit with a Cu-Kα radiation source (λ =1.54 Å) was used to ascertain the phase composition and crystal structure. The scanning process was conducted at a rate of 0.02° min^{-1}. A micro-Raman spectrometer (STR, India) was used to measure the Raman spectra. The thin oxide layer formed during the dealloying process was examined using X-ray photoelectron spectroscopy (XPS) (1.486 keV, Scienta Omicron Nanotechnology) with a monochromatic Al-Kα X-ray source. The acquired spectra were subsequently deconvoluted and analysed using CasaXPS software (V2.3). Additionally, the specific surface area was calculated using Brunauer–Emmett–Teller (BET) (Autoabsorb 6100/Anton Paar) analysis. The mechanical strength of the developed electrode was investigated using the universal testing machine (UTM) (Instron 3366, US).

2.5 Electrochemical characterization

The electrochemical characteristics of the prepared electrode were evaluated using a conventional three-electrode configuration with a Biologic VSP-3e potentiostat. The SM//NCM/O electrode was used as the working electrode, while a high-purity graphite rod acted as the counter electrode. A saturated calomel electrode (SCE) was used as the reference electrode, and 1 M KOH solution served as the electrolyte medium. Cyclic voltammetry (CV) measurements were performed at scan rates of 1 to 30 mV s^{-1}. Subsequently, galvanostatic charge–discharge (GCD) tests were carried out at current densities of 3 to 20 mA cm^{-2}. Areal capacitance was determined by analyzing the discharge duration alongside the current density. Furthermore, electrochemical impedance spectroscopy (EIS) was performed at the open-circuit potential (E_{OCP}) within a frequency range from 0.01 Hz to 100 kHz, employing a 10 mV AC voltage

stimulus. The collected data were fitted using an Echem Analyst 7.03 to generate an equivalent electrical circuit (EEC). Additionally, symmetric supercapacitor (SC) cells were constructed using SM//NCM/O electrodes for both the cathode and anode sides, a cellulose-based NKK separator, and a 3 M KOH electrolyte solution. The electrochemical performance of these symmetric SCs was investigated based on their total electrode area. CV tests were conducted at scan rates of 5 to 40 mV s^{-1}, while GCD measurements were performed at current densities of 1 to 6 mA cm^{-2}. The VSP-3e potentiostat was used to acquire both the charge–discharge profiles and the cyclic voltammograms within a voltage range of 0–1.5 V. Cycling stability was further evaluated by repeating 10 000 charge–discharge cycles at a current density of 4 mA cm^{-2}.

3. Results and discussion

3.1 Microstructure

The synthesis procedure for the NCM/O powder electrode is illustrated in Fig. 1. The NCM alloy was dealloyed in $(NH_4)_2SO_4$ solution to produce multicomponent nano-porous oxide powder (NCM/O). The NCM/O powder was then drop cast over 20 μm thick stainless steel mesh (Fig. S1) to fabricate a flexible electrode. The surface morphology of the as-synthesized NCM/O powder, as observed by FESEM, is shown in Fig. 2(a–b). A low magnification image shows a uniform porous structure of the powder particles (Fig. 2a) as a result of selective dealloying. A high magnification image reveals that the powder structure is flaky and nano-porous (Fig. 2b). A TEM image of the powder particle confirms the presence of fine nano-needles on a flake surface (Fig. 2c). The TEM EDS line scan analysis of the NCM/O powder is shown in Fig. 2d, while its elemental mapping is shown in Fig. 2e. The EDS analysis indicates a minimal Mn atomic fraction, which is attributed to its selective leaching from the Ni–Cu–Mn alloy system. Furthermore, the powder particle core was found to be enriched with metallic Ni and Cu, while its shell has a high oxide fraction. The EDS analysis also indicates enrichment of its outer surface with CuO nano-needles. The fabricated electrode was found to be super-flexible (Fig. S2). In addition, the electrode demonstrated appreciable mechanical strength, as determined through uniaxial tensile testing, wherein the electrode showed an ultimate tensile strength of 68.57 MPa along with 2.8 percentage elongation (Fig. S3).

The surface area of the developed nano-porous NCM/O powder was obtained using BET analysis. The resulting nitrogen adsorption–desorption isotherm (Fig. 3a) exhibits a Type IV curve with an H3-type hysteresis loop, indicative of a mesoporous structure.[22–24] The pore size distribution, shown in the inset of Fig. 3a, reveals that the majority of the pores are smaller than 20 nm. The specific surface area of the NCM/O powder, as determined by BET analysis, is calculated to be 9.4 m^2 g^{-1}. The crystal structure of the NCM/O powder was analysed using XRD, as shown in Fig. 3b. The diffraction peaks observed at 43.9°, 51.17°, and 74.9° correspond to a single-phase face-centered cubic (FCC) structure, while the peaks at 36.7° and 61.6° indicate the presence of a rock-salt type oxide.[25] A peak near ~36.8° corresponds to MnO_2 (JCPDS: 00-044-0141), while a peak at ~43.8° indicates NiO (JCPDS: 04-0835). Furthermore, a peak at ~51.1° corresponds to Mn_2O_3 (JCPDS: 06-0540), while a peak at ~61.6° and 74.8° belongs to CuO (JCPDS: 01-089-2529) and MnO (JCPDS: 00-075-1090), respectively. The broadening of several peaks can be attributed to the nanoporous nature of the material, which results from the selective removal of Mn. Furthermore, XPS analysis was conducted to investigate the surface composition and oxidation states of the

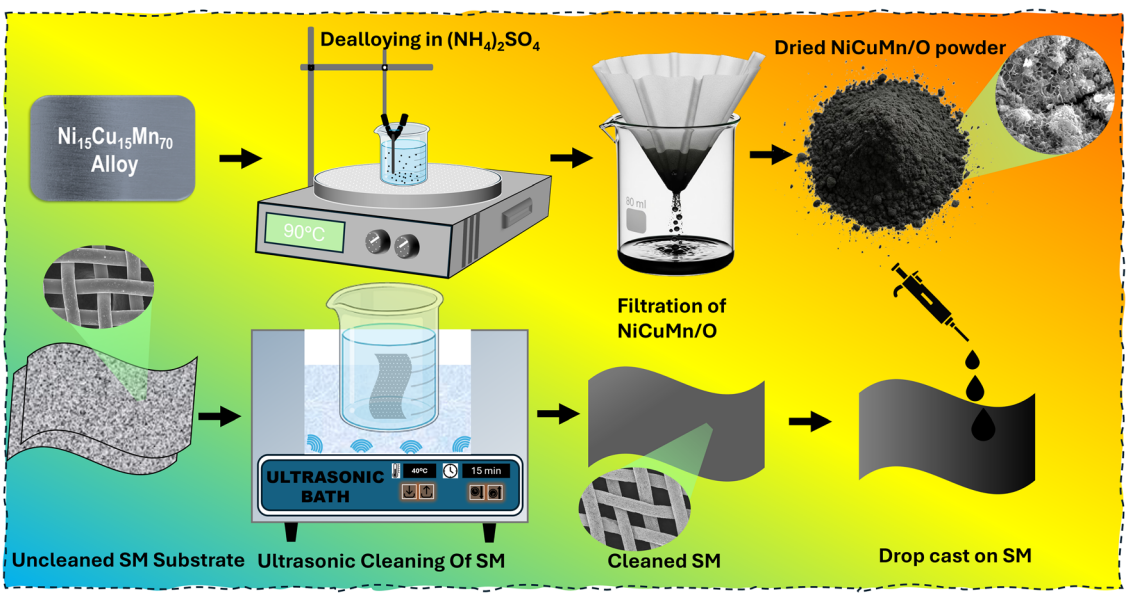

Fig. 1 Schematic illustration of the step-by-step fabrication process of the SM//NCM/O electrode.

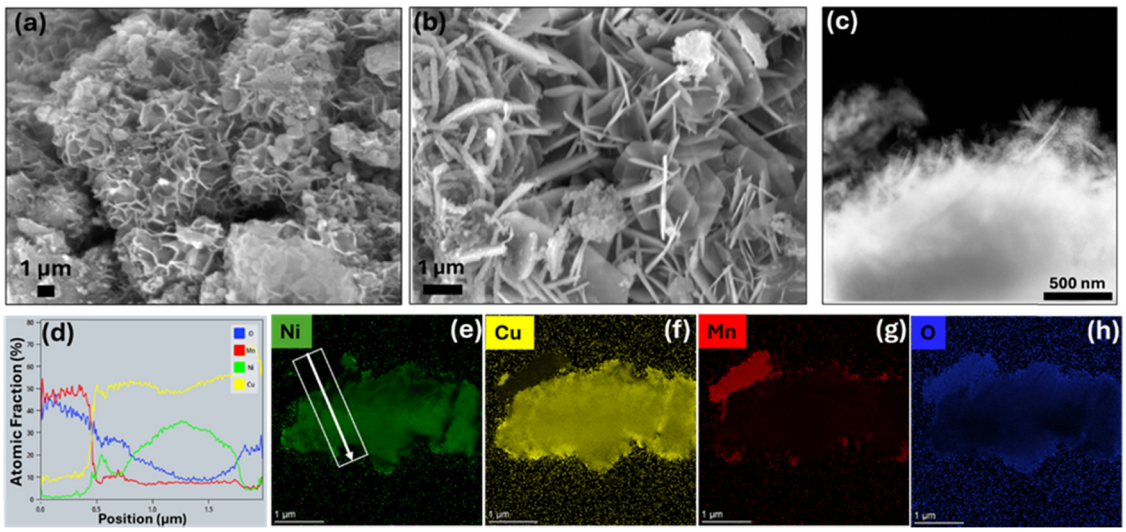

Fig. 2 (a) and (b) FESEM images of NiCuMn/O powder, (c) TEM image of NiCuMn/O powder, (d) line scan showing elemental distribution, and (e)–(h) EDS mapping of all the elements.

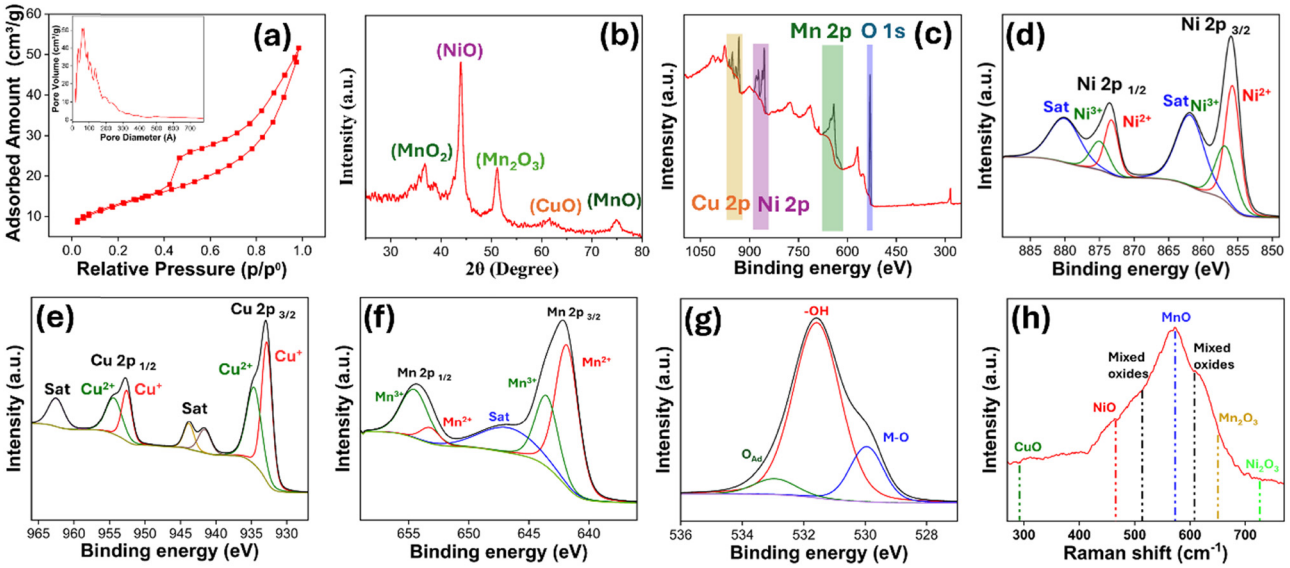

Fig. 3 (a) Nitrogen adsorption–desorption isotherm, and the inset of (a) shows pore size distribution, (b) XRD pattern, (c) XPS survey spectra, high-resolution XPS spectra of (d)–(g) Ni 2p, Cu 2p, Mn 2p, and O 1s, and (h) Raman spectra.

NCM/O powder. The XPS survey spectra were calibrated using the C 1s peak at 284.6 eV. The survey spectrum (Fig. 3c) confirms the presence of Ni, Cu, Mn, and O elements in the NCM/O powder. In the high-resolution XPS spectrum of Ni 2p (Fig. 3d), the peaks at 855.8 eV and 873.2 eV correspond to Ni^{2+}, while the peaks at 856.9 eV and 875.1 eV correspond to Ni^{3+}. Additionally, two satellite peaks are observed at 861.9 eV and 880.2 eV.[26] In the high-resolution XPS spectrum of Cu 2p (Fig. 3e), the peaks at 932.8 eV and 952.6 eV correspond to Cu^{+}, while the peaks at 934.67 eV and 954.47 eV are attributed to Cu^{2+}. Additionally, a satellite peak observed at 941.67 eV is associated with Cu^{+}, whereas the satellite peaks at 943.88 eV and 962.58 eV confirm the presence of Cu^{2+}.[27] Fig. 3f presents the high-resolution XPS spectrum of Mn 2p. The peaks observed at 641.87 eV and 653.38 eV are attributed to Mn^{2+}, while the peaks at 643.68 eV and 654.66 eV correspond to Mn^{3+}. Additionally, a satellite peak at 642.17 eV further confirms the presence of Mn^{2+}.[28] Fig. 3g displays the high-resolution XPS spectrum of O 1s. The peaks at 529.95 eV, 531.6 eV, and 532.95 eV are attributed to lattice oxygen in metal oxides (M–O), surface hydroxyl groups (–OH), and adsorbed oxygen species, respectively.[29] Furthermore, the Raman spectrum (Fig. 3h) was analysed to reconfirm the chemical species present on the specimen. Characteristic peaks observed at 290,

465, 573, 650, and 730 cm^{-1} correspond to CuO, NiO, MnO, Mn_2O_3, and Ni_2O_3, respectively, supporting the findings from the XPS analysis. Additionally, peaks at 514 and 608 cm^{-1} are attributed to the presence of mixed metal oxides.[30]

3.2 Electrode performance

The electrochemical performance of the flexible SM//NCM/O electrode was evaluated using a conventional three-electrode configuration. In this setup, the SM//NCM/O electrode served as the working electrode, a graphite rod acted as the counter electrode, and a saturated calomel electrode (SCE) was used as the reference. All measurements were conducted in a 1 M KOH aqueous electrolyte. Cyclic voltammetry (CV) tests were conducted at various scan rates ranging from 1 to 30 mV s^{-1} (Fig. 4a). The CV curves exhibited a wide stable window of 1.5 V between −1.0 V and 0.5 V. The quasi-rectangular shape of the CV curve combined with multiple distinct redox peaks is indicative of a hybrid charge storage mechanism involving both electric double-layer capacitance and surface-confined faradaic reactions. Notably, cathodic peaks appear around –0.4 V and –0.1 V, while prominent anodic responses are observed at –0.8 V, –0.35 V, and 0.26 V. The anodic peak on the positive potential window is attributed to the Ni^{2+}/Ni^{3+} redox couple. The cathodic signal at –0.8 V corresponds to the reduction of Cu^{2+} to Cu^{+}. The remaining redox features are likely associated with the synergistic electrochemical interactions arising from the mixed metal oxides present in the electrode material. The intensity and area under the CV curves increased with the scan rate, while the drift in the peak position was minimum, indicating good reversibility and fast redox kinetics.

Galvanostatic charge–discharge (GCD) testing was carried out at a series of current densities ranging from 3 to 20 mA cm^{-2} (Fig. 4b). The resulting GCD curves revealed nonlinear charge–discharge profiles with evident plateau, further confirming the hybrid nature of the electrode. The specific capacitance was calculated from the discharge segment of the GCD curves using the relation $C = I{\cdot}\Delta t/\Delta V$, where I is the areal current density, Δt is the discharge time and ΔV is the potential window. The maximum specific capacitance achieved was 1614 mF cm^{-2} at a current density of 3 mA cm^{-2}. Notably, even at a high current density of 20 mA cm^{-2}, the electrode offers a specific capacitance of 1213 mF cm^{-2} (Fig. S4), reflecting excellent rate capability and rapid ion/electron transport within the electrode. To further evaluate the dominant charge storage behavior, the relationship between peak current (i) and scan rate (v) was analyzed using the power law equation:

$$i = av^b$$

where a and b are the constants. The slope (b-value) of the log(i) *vs.* log(v) plot was calculated to be 0.7 (Fig. 4c), which suggests that the charge storage is primarily diffusion-controlled rather than purely capacitive. A b-value close to 0.5 typically signifies a battery-type diffusion-controlled process, while a b-value near 1.0 reflects ideal surface-controlled capacitive behavior. Hence, the observed value of 0.7 confirms the mixed nature of energy storage, where faradaic redox reactions occurring within the bulk or interior of active materials contribute significantly to the overall capacitance. To further quantify the contributions from each mechanism, the total current at a given potential $i(V)$ was separated into capacitive and diffusion-controlled components using the following relation:

$$i(V) = k_1v + k_2v^{1/2}$$

where k_1v represents the capacitive contribution and $k_2v^{1/2}$ accounts for the diffusion-controlled contribution. By plotting

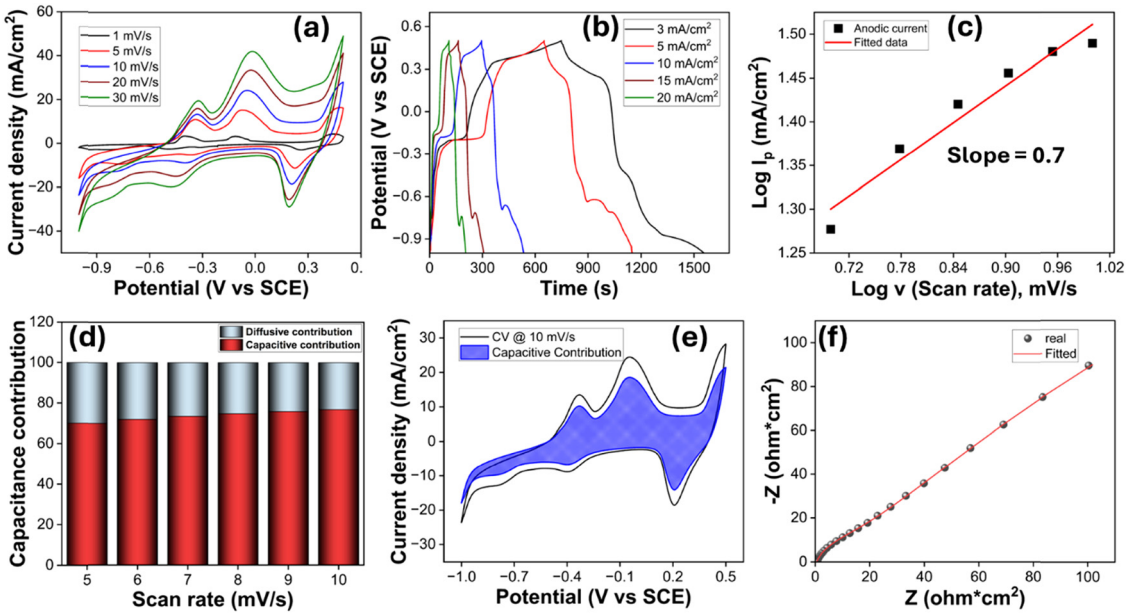

Fig. 4 Three-electrode electro-chemical data of the SM//NCM/O electrode: (a) cyclic voltammetry curves at different scan rates, (b) GCD curves at different current densities, (c) log I_p *vs.* log v graph, (d) bar plot of capacitance contributions at different scan rates, (e) capacitance contribution at 10 mV s^{-1} CV, and (f) the Nyquist plot.

$i(V)/v^{1/2}$ *versus* $v^{1/2}$, the constants k_1 and k_2 can be extracted. This method, often referred to as Dunn's method, allows the capacitive and diffusive contributions to be estimated at various scan rates. Fig. 4d presents the contribution percentage graph at different scan rates. At 5 mV s^{-1}, the capacitive contribution was calculated to be ~70%, while the remaining 30% originated from diffusion-controlled processes. As the scan rate increased from 5 to 10 mV s^{-1}, the capacitive contribution increased steadily up to ~77%. Fig. 4e shows the capacitive and diffusive contributions for CV performed at 10 mV s^{-1}. EIS was performed to evaluate the charge transport properties and interfacial behavior of the flexible hybrid electrode. The EIS measurement was carried out over a frequency range of 0.01 Hz to 100 KHz with an applied AC amplitude of 10 mV. The Nyquist plot (Fig. 4f) modeled with an equivalent electrical circuit (EEC) (Fig. S5) reveals key insights into the resistive and capacitive elements within the system. In the high-frequency region, the intercept on the real axis represents the solution resistance (R_s). The very low R_s value of 0.63 Ω indicates fast ion transport within the electrolyte and negligible ohmic losses arising from the specimen. To the best of our knowledge, only two published studies have reported EIS measurements for the same material system and electrolyte used in this work. Kang *et al.*[31] reported a solution resistance of 35 Ω, while Zhang *et al.*[30] reported a value of 2.5 Ω. In our measurements, the solution resistance was significantly lower, at 0.63 Ω. Such a low R_s confirms that the electrolyte and electrode surface are well integrated, which is essential for minimizing voltage drops during rapid charge–discharge processes.

The depressed semicircle observed in the mid-to-high frequency region corresponds to the charge-transfer resistance (R_{p1}), which captures the kinetics of faradaic reactions or surface redox processes occurring at the electrode–electrolyte interface. The small R_{p1} value suggests that electrons can be rapidly transferred between the active material and the substrate during charging and discharging. This improved interfacial charge transfer is enabled by (i) the continuous conductive network formed by the hybrid architecture, (ii) the intimate bonding between active materials and the flexible current-collecting matrix, and (iii) efficient electrolyte penetration and wetting due to the superhydrophilic nature of the electrode (Video S1). Altogether, these factors reduce interfacial barriers and facilitate fast electrochemical kinetics. In the low-frequency region, the plot transitions into a nearly vertical line, characteristic of rapid ion diffusion and good electrolyte accessibility to redox-active sites, critical for sustaining performance at high rates. This behaviour can be attributed to the porous architecture, high surface area, superhydrophilic nature and well-integrated conductive framework of the hybrid electrode. The porosity and interconnected channels facilitate fast electrolyte penetration and ion diffusion throughout the electrode, while the high surface area provides abundant redox-active sites accessible to electrolyte ions. Overall, the combination of low R_s, low R_{p1}, and the near-vertical low-frequency response signifies that the flexible hybrid electrode possesses (i) excellent ionic and electronic conductivity, (ii) fast interfacial charge-transfer kinetics, and (iii) highly accessible, well-wetted pores. These features collectively contribute to enhanced rate capability, reduced internal resistance, and improved cycling stability, ultimately translating into superior electrochemical performance for the flexible supercapacitor.

3.3 Device performance

The electrochemical performance of the assembled FHS was systematically evaluated in a two-electrode configuration. The device was assembled using two identical electrodes (SM//NCM/O), separated by a cellulose-based NKK separator dipped in 3 M KOH solution.

Fig. 5a illustrates the CV curves recorded at scan rates ranging from 5 to 50 mV s^{-1} (Fig. 5a). These curves exhibit a hybrid shape, combining nearly rectangular features with distinct redox peaks, which indicates the simultaneous presence of electric double-layer capacitance and faradaic processes. The CV profile indicates that the device maintained the wide and stable potential window of 1.5 V. Fig. 5b presents the GCD curves obtained at current densities between 1 and 6 mA cm^{-2}. Areal specific capacitance values were calculated from the discharge times derived from these GCD measurements, as shown in the Fig. S6. Impressively, the device demonstrated high areal capacitance, ranging from 414.6 mF cm^{-2} at 1 mA cm^{-2} to 312 mF cm^{-2} at 6 mA cm^{-2}. The GCD curves also reveal the hybrid nature of the device, characterized by excellent charge–discharge reversibility and a negligible IR drop, even at higher current densities. These attributes point to low internal resistance and efficient charge transfer kinetics. Moreover, the stable performance across the extended 1.5 V window further validates the device's electrochemical reliability. This broad voltage range exceeds the typical limit (~1 V) for symmetric devices and plays a crucial role in boosting energy density, as energy scales with the square of the voltage ($E = 1/2CV^2$). The device exhibits an outstanding energy density of 129.58 μWh cm^{-2} at a current density of 1 mA cm^{-2}, which remains appreciably high at 97.5 μWh cm^{-2} even at 6 mA cm^{-2}. Additionally, it delivers a strong power density, reaching 750 μW cm^{-2} at 1 mA cm^{-2} and increasing to 4500 μW cm^{-2} at 6 mA cm^{-2}. These results compare favourably with several previously reported studies, reflecting the promising performance of the device. The Ragone plot (Fig. 5c) provides a comparative analysis between the performance of the present device and those reported in earlier studies.[32–39] To assess long-term operational stability, the device was subjected to continuous cycling at a current density of 4 mA cm^{-2} for 10 000 cycles. The XRD patterns (Fig. S7) of both specimens (before and after cycling) were found to be nearly identical, indicating that no significant structural changes occurred during long-term cycling.

Impressively, it retained 94.7% of its initial capacitance, as illustrated in Fig. 5d, demonstrating excellent cycling stability. These findings confirm the robustness of the electrode material under prolonged electrochemical operation. Overall, the study establishes this material system as a highly promising

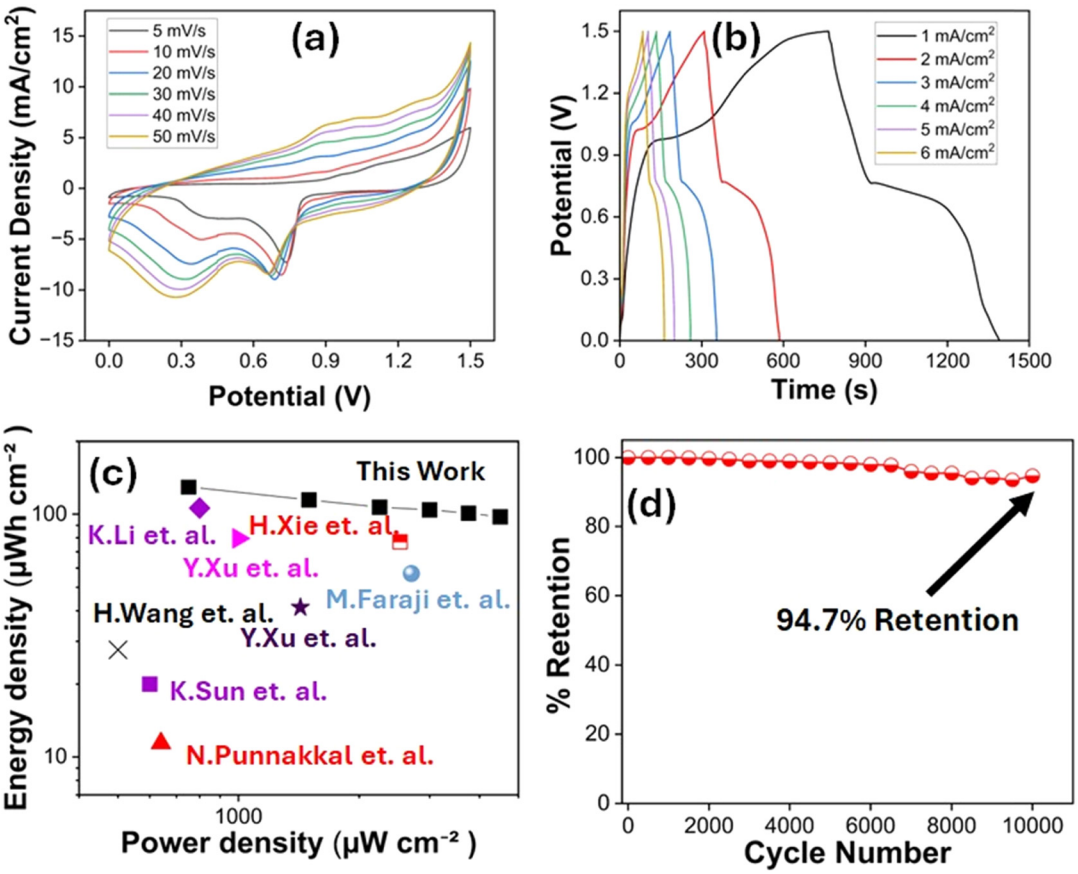

Fig. 5 Electro-chemical data of the fabricated FHS: (a) cyclic voltammetry curves at different scan rates, (b) GCD curves at different current densities, (c) Ragone plot (comparison of the areal energy density and power density of the FHS), and (d) cycling stability of the FHS over 10 000 charge–discharge cycles.

candidate for next-generation high-performance flexible energy storage systems.

3.4 Practical applications

To demonstrate the practical applicability of the fabricated flexible supercapacitor, two devices were connected in both series and parallel configurations. The CV and GCD curves for both series and parallel arrangements are shown in Fig. 6a and b, respectively. In the series arrangement, the combined device exhibited an extended voltage window of 3 V, as observed from the CV curves, while maintaining an almost similar current response. This is crucial for powering devices that require higher operating voltages. In the parallel configuration, the CV curves showed an increased current response in the same voltage window, indicating enhanced charge storage capability. Similarly, GCD measurements revealed that the series connection resulted in an increased potential window, whereas the parallel arrangement exhibited increased discharge durations at a constant voltage window, confirming improved capacity. These results collectively demonstrate the scalability and practical utility of the devices for real-world energy storage applications. The electrochemical testing of the fabricated supercapacitor device under bending conditions was carried out to assess its mechanical robustness and performance stability under real working conditions. The CV data for the device while it was subjected to various bending angles, including flat (0°), 45°, 90°, 135°, and 180°, are shown in Fig. 6c. The CV curves retained their shape with minimal distortion across all bending states, indicating excellent structural integrity and stable electrochemical behaviour. Even after multiple bending cycles at 135°, the CV profiles remained nearly unchanged, further confirming the device's mechanical robustness (Fig. S8). These results demonstrate that the device possesses superior flexibility and is well-suited for applications in next-generation wearable and portable energy storage systems.

After validating the superior flexibility and electrochemical performance of the fabricated flexible supercapacitor, we proceeded to demonstrate its practical integration into wearable electronic devices. As a proof-of-concept, we designed a wristwatch strap embedded with a flexible SC module to showcase its real-world applicability. For this purpose, four flexible electrodes of dimensions 21 cm × 2 cm (Fig. 6d) were fabricated. These fabricated electrodes were used to assemble two supercapacitor devices. These supercapacitors were assembled in a series configuration to enhance the overall output voltage of the device, aligning with the typical power requirements of wearable electronics. The resulting flexible SC was then used as a wristwatch strap (FSWS) of a wristwatch. The pre-installed

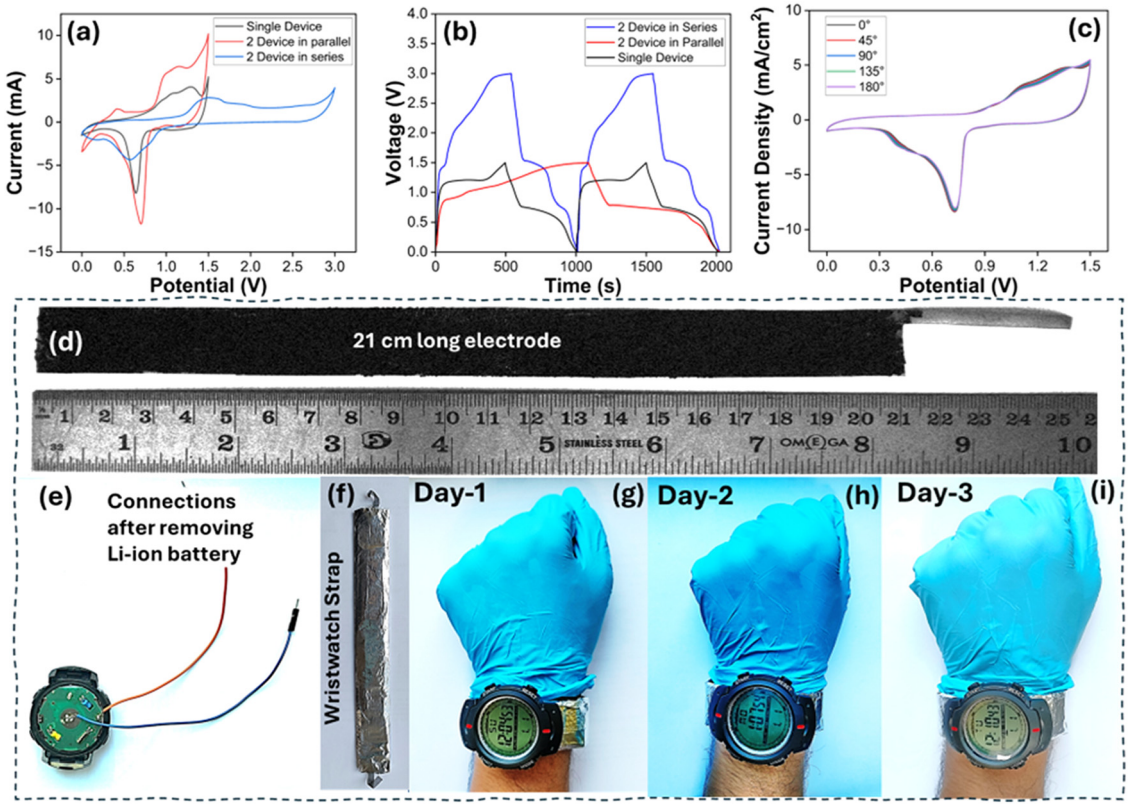

Fig. 6 (a) CV plots for two FHS devices connected in series and parallel, (b) GCD plots for two FHS devices connected in series and parallel, (c) CV plots of FHS at different bending angles, digital photographs of (d) the as-prepared long electrode, (e) wristwatch connections after removing the Li-ion battery, (f) the as-prepared FSWS, and (g)–(i) running wristwatch for consecutive days.

Li-ion battery in the wristwatch was carefully removed, as shown in Fig. 6e, and replaced with the in-house fabricated FSWS (Fig. 6f). This integration effectively powered the wristwatch, demonstrating the practical viability of the flexible SC in wearable electronics. Notably, the FSWS powered wristwatch operated continuously, and the snapshots for first three days are shown in Fig. 6(g–i). The video of the running wristwatch is shown in Video S2 in the SI, confirming the device's capability to serve as a sustainable energy source for low-power wearable applications.

4. Conclusion

In summary, a TMO based flexible supercapacitor electrode was successfully developed and its electrochemical performance was assessed using a three-electrode setup. The electrode exhibited a specific capacitance of 1614 mF cm^{-2} at a current density of 3 mA cm^{-2} and retained ~75% of the specific capacitance even at a high current density of 25 mA cm^{-2}. Following this, a symmetric supercapacitor device was assembled using two identical electrodes, which demonstrated stable operation with a device capacitance of 414.6 mF cm^{-2} at 1 mA cm^{-2} and a voltage window of 1.5 V. The assembled supercapacitor exhibits excellent rate capability, retaining over 75% of its capacitance as the current density increases from 1 to 6 mA cm^{-2}. The device also showed exceptional cycling stability, retaining 94.7% of its initial performance after 10 000 charge–discharge cycles. Additionally, it delivered a high power density ranging from 750 μW cm^{-2} to 4500 μW cm^{-2}, along with an impressive energy density between 129.58 μWh cm^{-2} and 97.5 μWh cm^{-2}, confirming its suitability for practical energy storage. To further explore its real-world applicability, larger electrodes were fabricated and integrated as a flexible wristwatch strap. The custom-made supercapacitor strap successfully replaced the conventional Li-ion battery and was able to power the wristwatch continuously for several days. These results clearly demonstrate the promise of the TMO based fabricated flexible supercapacitor as a reliable, scalable, lightweight, high strength and bendable power source for wearable electronic applications.

Conflicts of interest

The authors declare no conflict of interest.

Data availability

Data are available upon request from the authors.

The data supporting this article have been included as part of the supplementary information (SI). Digital photograph showing thickness of flexible SM substrate (Fig. S1), digital photograph showing flexibility of the electrode (Fig. S2), stress

vs. strain curve for the electrode (S3), areal capacitance of the electrode at different current densities (Fig. S4), equivalent electrical circuit for modelling of impedance spectra (Fig. S5), areal capacitance of the FHS device at different current densities (Fig. S6), XRD spectra of the electrode before and after 10 000 cycles (Fig. S7), CV curves of the device in the multiple bending cycles at 135° (Fig. S8). See DOI: https://doi.org/10.1039/d5ma01187f.

References

1 Z. Jiang, W. Feng, Z. Lin, Y. Cai, M. Liu, X. Hu, X. Zeng, X. Liu, Y. Wu, Y. Zhang, L. Tian and N. Yi, One-pot construction of all-in-one flexible asymmetrical supercapacitors for extreme-condition applications, *Chem. Eng. J.*, 2024, **501**, 157553, DOI: 10.1016/j.cej.2024.157553.

2 K. Liu, T. Duan, F. Zhang, X. Tian, H. Li, M. Feng, R. Wang, B. Jiang and K. Zhang, Flexible electrode materials for emerging electronics: materials, fabrication and applications, *J. Mater. Chem. A*, 2024, **12**(32), 20606–20637, DOI: 10.1039/D4TA01960A.

3 Q. Xue, J. Sun, Y. Huang, M. Zhu, Z. Pei, H. Li, Y. Wang, N. Li, H. Zhang and C. Zhi, Recent Progress on Flexible and Wearable Supercapacitors, *Small*, 2017, **13**(45), 1701827, DOI: 10.1002/smll.201701827.

4 D.-Y. Kim, S. Radhakrishnan, S. Yu and B.-S. Kim, Polyacrylonitrile-grafted lignin copolymer derived carbon nanofibers as a flexible electrode for high-performance capacitive-energy storage, *Mater. Adv.*, 2023, **4**(15), 3215–3223, DOI: 10.1039/D3MA00194F.

5 Y. Cao, S. Sun, W. Li, Y. Chang, N. Gu, J. Yao and Y. Sun, Challenge and technological trends of flexible solid-state supercapacitors, *J. Energy Storage*, 2024, **97**, 112837, DOI: 10.1016/j.est.2024.112837.

6 S. Zhao, J. Li, D. Cao, G. Zhang, J. Li, K. Li, Y. Yang, W. Wang, Y. Jin, R. Sun and C.-P. Wong, Recent Advancements in Flexible and Stretchable Electrodes for Electromechanical Sensors: Strategies, Materials, and Features, *ACS Appl. Mater. Interfaces*, 2017, **9**(14), 12147–12164, DOI: 10.1021/acsami.6b13800.

7 S. A. Delbari, L. S. Ghadimi, R. Hadi, S. Farhoudian, M. Nedaei, A. Babapoor, A. Sabahi Namini, Q. V. Le, M. Shokouhimehr, M. Shahedi Asl and M. Mohammadi, Transition metal oxide-based electrode materials for flexible supercapacitors: A review, *J. Alloys Compd.*, 2021, **857**, 158281, DOI: 10.1016/j.jallcom.2020.158281.

8 K. Kang, X. Tang, J. Duan, B. Yang and J.-Y. Hu, Carbon Nanotubes Exfoliated HATN-COF for Efficient Supercapacitor Active Materials, *Energy Fuels*, 2025, **39**(1), 921–927, DOI: 10.1021/acs.energyfuels.4c04884.

9 S. Kumar, G. Saeed, L. Zhu, K. N. Hui, N. H. Kim and J. H. Lee, 0D to 3D carbon-based networks combined with pseudocapacitive electrode material for high energy density supercapacitor: A review, *Chem. Eng. J.*, 2021, **403**, 126352, DOI: 10.1016/j.cej.2020.126352.

10 K. Pal, V. Panwar, S. Bag, J. Manuel, J.-H. Ahn and J. K. Kim, Graphene oxide–polyaniline–polypyrrole nanocomposite for a supercapacitor electrode, *RSC Adv.*, 2015, **5**(4), 3005–3010, DOI: 10.1039/C4RA14614J.

11 J. V. Vaghasiya, K. Křípalová, S. Hermanová, C. C. Mayorga-Martinez and M. Pumera, Real-Time Biomonitoring Device Based on 2D Black Phosphorus and Polyaniline Nanocomposite Flexible Supercapacitors, *Small*, 2021, **17**(38), 2102337, DOI: 10.1002/smll.202102337.

12 S. Jayakumar, P. C. Santhosh, M. M. Mohideen and A. V. Radhamani, A comprehensive review of metal oxides (RuO2, Co3O4, MnO2 and NiO) for supercapacitor applications and global market trends, *J. Alloys Compd.*, 2024, **976**, 173170, DOI: 10.1016/j.jallcom.2023.173170.

13 M. Shao, J. Dong, Z. Ge, R. Ge, Y. Ge, X. Lv, M. Ouyang and C. Zhang, Flexible PEDOT/NiO@nickel foam composites materials for high-performance supercapacitors, *J. Polym. Sci.*, 2023, **61**(24), 3343–3352, DOI: 10.1002/pol.20230541.

14 S. P. Shaji, M. Mohanraj, V. Aravindan and M. Ulaganathan, High-Performance β-MnO2-Based Flexible and Binder-Free Asymmetric Supercapacitor, *ChemNanoMat*, 2025, 2500197, DOI: 10.1002/cnma.202500197.

15 R. S. Desai, V. S. Jadhav, P. S. Patil and D. S. Dalavi, Recent advances in hydrothermally and solvothermally grown Co3O4 nanostructures for electrochemical energy storage (EES) applications: a brief review, *Mater. Adv.*, 2024, **5**(3), 920–960, DOI: 10.1039/D3MA00806A.

16 A. Kumar, A. Thomas and H. S. Arora, Deformation-Mediated Surface Activation of a Ni–Cu–Mn Ternary Alloy System for Energy Storage in Supercapacitors, *Energy Fuels*, 2023, **37**(6), 4720–4725, DOI: 10.1021/acs.energyfuels.2c04361.

17 X. Zhu, Recent advances of transition metal oxides and chalcogenides in pseudo-capacitors and hybrid capacitors: A review of structures, synthetic strategies, and mechanism studies, *J. Energy Storage*, 2022, **49**, 104148, DOI: 10.1016/j.est.2022.104148.

18 M. Cui and X. Meng, Overview of transition metal-based composite materials for supercapacitor electrodes, *Nanoscale Adv.*, 2020, **2**(12), 5516–5528, DOI: 10.1039/D0NA00573H.

19 S. Kausar, M. Yousaf, S. Mir, N. S. Awwad, H. A. Alturaifi and F. Riaz, Mesoporous Materials: Synthesis and electrochemical applications, *Electrochem. Commun.*, 2024, **169**, 107836, DOI: 10.1016/j.elecom.2024.107836.

20 A. Kumar, A. Thomas and H. S. Arora, Single-step, in-situ fabrication of flower-like NiCuMn hybrid oxyhydroxide electrodes for enhanced supercapacitor performance, *Nanotechnology*, 2024, **35**(34), 345403, DOI: 10.1088/1361-6528/ad5209.

21 A. Kumar, M. Lastovich, B. Gwalani and H. Singh Arora, Carbon-Doped NiCuMn Supercapacitor with Excellent Energy Storage and Rate Capability, *Energy Technol.*, 2025, **13**(10), 2500260, DOI: 10.1002/ente.202500260.

22 Y. Shen, S. He, Y. Zhuang, S. Huang, C. Meng, A. Yuan, W. Miao and H. Zhou, Polypyrrole Template-Assisted Synthesis of Tubular Fe-NC Nanostructure-Based Electrocatalysts for Efficient Oxygen Reduction Reaction in Rechargeable

Zinc–Air Battery, *ACS Appl. Nano Mater.*, 2023, **6**(18), 16873–16881, DOI: 10.1021/acsanm.3c03056.

23 S. Qiang, J. Chen, S. Huang, H. Xu, X. Zhuo, H. Zhou, A. Yuan, H. Zhou and Y. Qiao, Hierarchically porous CoMn-N-doped carbon nanotubes as efficient electrocatalyst for oxygen reduction reaction, *J. Colloid Interface Sci.*, 2026, **701**, 138722, DOI: 10.1016/j.jcis.2025.138722.

24 S. Huang, Y. Shen, A. Li, H. Zhou, Y. Qiao, A. Yuan, H. Zhou and S. Zheng, Dual-template synthesis of CoNi alloy nanoparticles anchored on N-doped carbon nanotubes for efficient oxygen reduction reaction, *Int. J. Miner., Metall. Mater.*, 2025, **32**, 1–9, DOI: 10.1007/s12613-025-3190-y.

25 J. J. Gao, H. J. Qiu, Y. R. Wen, F. K. Chiang and Y. Wang, Enhanced electrochemical supercapacitance of binder-free nanoporous ternary metal oxides/metal electrode, *J. Colloid Interface Sci.*, 2016, **474**, 18–24, DOI: 10.1016/j.jcis.2016.03.028.

26 Y. Wang, S. Tao, H. Lin, S. Han, W. Zhong, Y. Xie, J. Hu and S. Yang, NaBH4 induces a high ratio of Ni3 +/Ni2+ boosting OER activity of the NiFe LDH electrocatalyst, *RSC Adv.*, 2020, **10**(55), 33475–33482, DOI: 10.1039/D0RA06617F.

27 L. S. Oh, J. Han, E. Lim, W. B. Kim and H. J. Kim, PtCu Nanoparticle Catalyst for Electrocatalytic Glycerol Oxidation: How Does the PtCu Affect to Glycerol Oxidation Reaction Performance by Changing pH Conditions?, *Catalysts*, 2023, **13**(5), 892, DOI: 10.3390/catal13050892.

28 T. Wu, Y. Du, Z.-J. Zuo, S. Li, J. Wu, J. Gao, T. Mu, Y.-C. Zhang and X.-D. Zhu, In@Mn_3O_4 with Rich Interface Low-Coordination Mn Active Sites for Boosting Electrocatalytic Nitrogen Reduction, *Adv. Funct. Mater.*, 2025, **35**(24), 2424142, DOI: 10.1002/adfm.202424142.

29 X. Yu, S. Wang, H. Xie, Z. Yi, J. Tang, H. Gao, H. Yang, L. Fang and A. Syed, Nano spinel NiAl2O4: structure, optical and photocatalytic performance evaluation and optimization, *J. Phys.: Condens. Matter*, 2024, **36**(10), 105201, DOI: 10.1088/1361-648X/ad1000.

30 S. Zhang, B. Du, T. Li, J. Sun, Y. Meng, Z. Zhang and J. Kang, Self-combustion induced hierarchical nanoporous alloy transition toward high area property electrode for supercapacitor, *J. Alloys Compd.*, 2022, **900**, 163443, DOI: 10.1016/j.jallcom.2021.163443.

31 J. Kang, A. Hirata, L. Chen, S. Zhu, T. Fujita and M. Chen, Extraordinary Supercapacitor Performance of a Multicomponent and Mixed-Valence Oxyhydroxide, *Angew. Chem., Int. Ed.*, 2015, **54**(28), 8100–8104, DOI: 10.1002/anie.201500133.

32 Y. Xu, Y. Zhang, Y. Meng, M. Xiao, Y. Cheng, X. Lu and F. Zhu, In situ preparation of nitrogen-doped carbon nanotubes on carbon cloth surface as binder-free flexible electrode materials for supercapacitors, *J. Mater. Sci.: Mater. Electron.*, 2023, **34**(6), 546, DOI: 10.1007/s10854-023-09976-6.

33 H. Wang, Q. Zhang, S. Chen, X. Liu, J. Liu, W. He and X. Liu, Highly Conductive Supramolecular Salt Gel Electrolyte for Flexible Supercapacitors, *ACS Appl. Mater. Interfaces*, 2024, **16**(41), 56170–56180, DOI: 10.1021/acsami.4c12666.

34 K. Sun, E. Feng, G. Zhao, H. Peng, G. Wei, Y. Lv and G. Ma, A Single Robust Hydrogel Film Based Integrated Flexible Supercapacitor, *ACS Sustainable Chem. Eng.*, 2019, **7**(1), 165–173, DOI: 10.1021/acssuschemeng.8b02728.

35 M. Faraji, R. Khalilzadeh Soltanahmadi, H. Mohammadzadeh Aydisheh and B. Mostafavi Bavani, 2.0-V flexible all-solid-state symmetric supercapacitor device with high electrochemical performance composed of MWCNTs-WO3-graphite sheet, *Ionics*, 2020, **26**(6), 3003–3013, DOI: 10.1007/s11581-020-03502-y.

36 N. Punnakkal, S. Naneena, C. P. Shyam Lal, A. Pradeep, T. G. Satheesh Babu and P. V. Suneesh, Nitrogen-doped graphene quantum dot embedded polyaniline for the fabrication of high-performance flexible supercapacitor with enhanced cycling stability, *J. Energy Storage*, 2024, **100**, 113527, DOI: 10.1016/j.est.2024.113527.

37 K. Li, B. Zhao, H. Zhang, H. Lv, J. Bai, H. Ma, P. Wang, W. Li, J. Si, X. Zhu and Y. Sun, 3D Porous Honeycomb-Like CoN-Ni3N/N-C Nanosheets Integrated Electrode for High-Energy-Density Flexible Supercapacitor, *Adv. Funct. Mater.*, 2021, **31**(28), 2103073, DOI: 10.1002/adfm.202103073.

38 Y. Xu, X. Yu, X. Wang, J. Yu and P. Huang, Application of additive-free, ultra-stable polyimide-derived porous carbon with controllable structure in flexible supercapacitors, *J. Energy Storage*, 2024, **103**, 114359, DOI: 10.1016/j.est.2024.114359.

39 H. Xie, S. Tang, J. Zhu, S. Vongehr and X. Meng, A high energy density asymmetric all-solid-state supercapacitor based on cobalt carbonate hydroxide nanowire covered N-doped graphene and porous graphene electrodes, *J. Mater. Chem. A*, 2015, **3**(36), 18505–18513, DOI: 10.1039/C5TA05129K.